



Cite this: *New J. Chem.*, 2025, 49, 13049

Tunable microwave absorbers: divalent ion-doped soft magnetic ferrite/CNT composites with customizable electromagnetic properties†

Zhihao Geng,  Yujie Yang,* Hao Li, Zhenyu Zhang and Hongyu Ding

This study investigated the influence of different metal cation substitutions in nickel–zinc ferrite composites on their magnetic and microwave absorption properties. $\text{Ni}_{0.4}\text{Zn}_{0.4}\text{Me}_{0.2}\text{Fe}_{1.94}\text{Cr}_{0.01}\text{O}_4/\text{CNT}$ composites (Me = Mg, Co, Ni, Cu, and Zn) were synthesized *via* solid-phase reaction and ultrasonication, followed by comprehensive characterization of their microstructure, magnetic behavior, and microwave absorption performance. X-ray diffraction (XRD) analysis revealed cation-dependent variations in crystallite size. Scanning electron microscopy (SEM) demonstrated uniform dispersion of carbon nanotubes (CNTs) within the ferrite matrix, accompanied by robust interfacial bonding. Vibrating sample magnetometer (VSM) measurements indicated that Zn^{2+} -doped samples exhibited the lowest saturation magnetization (61.53 emu g^{-1}), whereas their Co^{2+} -doped counterparts achieved the highest value (75.97 emu g^{-1}). Vector network analyzer (VNA) results showed that Cu^{2+} -doped composites attained a minimum reflection loss of -46.32 dB at 1.4 mm thickness, while Co^{2+} -doped samples displayed the broadest effective absorption bandwidth (4.3 GHz) at 1.9 mm thickness.

Received 6th May 2025,
Accepted 24th June 2025

DOI: 10.1039/d5nj01915j

rsc.li/njc

1. Introduction

Electromagnetic pollution is becoming more serious due to the rapid development of electronic technology and the use of electromagnetic weapons in modern warfare. To mitigate this issue, designing a new wave-absorbing material that is easy to prepare and suitable for mass production has become increasingly important.^{1,2}

Microwave-absorbing materials (MAMs) are specifically designed to attenuate propagating electromagnetic radiation by converting incident energy into thermal dissipation *via* intrinsic loss mechanisms. MAMs are systematically categorized into two dominant classes: magnetically lossy materials and dielectric loss-dominated carbon-based systems, as extensively documented in seminal studies.^{3,4} Ferrites have ascended as preeminent magnetic absorbers due to their exceptional magnetic permeability, economic viability, and sustainable resource availability, with spinel-type architectures particularly prevalent in contemporary research.⁵ Spinel ferrite is a typical magnetic material. Spinel ferrites are typically represented by the general formula AB_2O_4 , where the A-site is occupied by

divalent cations and the B-site is predominantly occupied by Fe^{3+} ions. A distinctive feature of these materials lies in the tunability of their magnetic properties (saturation magnetization and coercivity) through compositional adjustments (A/B-site ion types and ratios), synthesis methods, and sintering conditions (time, atmosphere, and temperature). This tunability is intrinsically linked to their unique crystal structure.^{5,6} Ma *et al.*⁷ doped nano Ni–Zn ferrite powders with varying concentrations of Co^{2+} , Mn^{2+} , and Cu^{2+} using a hydrothermal process and found that adding an appropriate amount of Cu^{2+} enhances the material's absorption capabilities. Somayeh *et al.*⁸ tailored the morphology of the CaFe_2O_4 spinel phase using dendrimer templates, achieving a remarkable absorption bandwidth and a reflection loss of -70.11 dB . Separately, Reza *et al.*⁹ incorporated lanthanum doping into CuFe_2O_4 with varying molar ratios, attaining a maximum reflection loss of -73.95 dB and an effective bandwidth of 7.30 GHz . Huang *et al.*¹⁰ produced nanoscale Ni–Zn ferrite by electrostatic spinning, and at a Ni^{2+} content of 0.5, they obtained a minimum absorption peak of -14.1 dB . Carbon materials are now the focus of microwave absorption applications because of their exceptional qualities, low density, thin-matched thickness, and a high dielectric constant.¹¹

It is well known that microwave absorbers must meet two specifications: strong electromagnetic attenuation and good impedance matching. Excellent microwave absorption performance is mainly due to the effective complementarity of

Engineering Technology Research Center of Magnetic Materials, Anhui Province, School of Materials Science and Engineering, Anhui University, Hefei 230601, P. R. China. E-mail: loyalty-yyj@163.com

† Electronic supplementary information (ESI) available. See DOI: <https://doi.org/10.1039/d5nj01915j>

complex permittivity and permeability so that a single magnetic or dielectric loss in the absorber can produce only a weak impedance match.¹² Ferrite composites are created for this reason. The novel g-C₃N₄ nanorods/Cu₃BiS₃ composite fabricated by Paria *et al.*¹³ *via* hydrothermal synthesis significantly enhances visible-light absorption while improving wastewater contaminant remediation. Mustaffa *et al.*¹⁴ fabricated multi-walled CNT/Ni_{0.5}Zn_{0.5}Fe₂O₄ composites by mechanical alloying, which exhibited a maximum reflection loss of −19.34 dB at 8.46 GHz and 1.5 GHz frequencies and bandwidths, with an absorber thickness of 3 mm. Chahar *et al.*¹⁵ used coprecipitation and physical mixing techniques to create the MWCNTs/Ni_{0.5}Zn_{0.5}Fe₂O₄ nanocomposites, which had a reflection loss value of −51.2 dB in the X-band at about 11.2 GHz. Wang *et al.*¹⁶ developed carbonized cellulose paper/HEAs-Mn_{2.15} composites that achieve efficient electromagnetic wave absorption of −51.35 dB at an ultra-thin thickness of 1.03 mm. By extending carbon sources to biomass categories, core-shell heterointerfaces between HEAs and carbon matrices were constructed through a modified carbothermal shock method. Seyed *et al.*¹⁷ achieved a reflection loss of −71.32 dB at 23.06 GHz through morphology-controlled MgFe₂O₄ composited with PET. Separately, Reza *et al.*¹⁸ synthesized ZnAl₂O₄ nanomaterials with varied morphologies *via* sol-gel and solvothermal methods, demonstrating exceptional absorption performance with PVDF composites reaching a −95.63 dB reflection loss. In another study, Reza *et al.*¹⁹ obtained a −79.08 dB reflection loss using MWCNTs composited with Zn_{0.25}Co_{0.75}Fe₂O₄.

This study employs nickel-zinc ferrite as the matrix, utilizing Zn²⁺ and Ni²⁺ as benchmark dopants for performance comparison while incorporating Mg²⁺, Co²⁺, and Cu²⁺ for synergistic functionalization: Mg²⁺ occupies the tetrahedral A-sites as a non-magnetic species to significantly enhance resistivity and suppress eddy current losses; Co²⁺ stabilizes high-frequency magnetic responses through magnetocrystalline anisotropy modulation; whereas Cu²⁺ optimizes charge transport characteristics *via* its superior electrical conductivity. Based on this complementary mechanism, these five ions were selected for ferrite doping, followed by integration with carbon nanotubes to fabricate high-performance electromagnetic wave-absorbing composites. This study synthesized nickel-zinc ferrite doped with five divalent metal cations using solid-state synthesis. Subsequently, composites of ferrite and carbon nanotubes (CNTs) were fabricated through ultrasonic processing. The morphology, magnetization strength, and microwave absorption properties were systematically analyzed. The results indicate that Cu²⁺- and Co²⁺-doped ferrite/CNT composites effectively balance magnetic-dielectric loss synergies, enhancing impedance matching and optimizing microwave absorption performance. The primary objective of this work is to elucidate the influence of divalent metal cation doping in ferrite/CNT composites on their microwave absorption behavior, intending to guide the development of high-performance microwave-absorbing materials.

2. Experimental procedure

2.1. Preparation

This study synthesizes a composite material *via* a two-step procedure, beginning with the synthesis of ferrite. The Ni_{0.4}Zn_{0.4}Me_{0.2}Fe_{1.94}Cr_{0.01}O₄ (Me = Mg, Co, Ni, Cu, and Zn) ferrite was synthesized *via* a solid-phase sintering protocol. Initially, stoichiometric quantities of high-purity Fe₂O₃ (99.9%), NiO (99%), ZnO (99%), MgO (98%), Co₃O₄ (99.9%), CuO (99%), and Cr₂O₃ (99%) were precisely weighed, with all reagents purchased from Aladdin Industrial Corporation (China). The mixture was subjected to planetary ball milling for 3 h at 230 rpm using deionized water and stainless-steel grinding media, followed by calcination at 860 °C for 6 h in an electric arc furnace. Subsequently, a 10 wt% polyvinyl alcohol (PVA) binder and 0.05 wt% zinc stearate (as a release agent) were incorporated into the pre-sintered powders, which were then compacted into toroidal shapes and sintered at 1170 °C for 8 h. In the second step, 10 g of ferrite powder and 0.65 g of carbon nanotubes (CNTs) were dispersed in 100 mL of anhydrous ethanol, followed by ball-milling at 100 rpm for 1 h with mechanical crushing to ensure homogeneity. The mixture was then subjected to ultrasonic oscillation until complete ethanol evaporation, yielding the ferrite/CNT composite. This composite was uniformly blended with paraffin at a 40 wt% ratio for electromagnetic characterization.

In this article, A1 refers to Mg²⁺-doped, A2 to Co²⁺-doped, A3 to Ni²⁺-doped, A4 to Cu²⁺-doped, and A5 to Zn²⁺-doped.

2.2. Characterization

Samples are analyzed using an X-ray diffractometer (XRD, Smart Lab, Japan Design). The morphology is characterized using transmission electron microscopy (TEM, TE02-DT) and scanning electron microscopy (SEM, Sigma-500, Carl Zeiss, Germany). Analysis of the sample elements is performed with an energy spectrometer (EDS, Sigma-500, Carl Zeiss, Germany). Hysteresis lines of the samples are measured using a vibrating sample magnetometer (VSMS-7404, Lakeshore Region, USA). The microwave absorption performance is tested using a vector network analyzer (VNA, MS4647B).

3. Results and discussion

3.1. Phase and structure analysis

The phase composition of carbon nanotubes (CNTs) and ferrite composites as analysed using an X-ray diffractometer (XRD) is displayed in Fig. 1. CNTs at $2\theta = 25.8^\circ$ show a strong diffraction peak matching the (003) crystal face of C (ICDD# 01-073-5918). The XRD curves of the five composite samples share the same trend and all show strong diffraction peaks at $2\theta = 35.4^\circ$ and match all the crystal faces in Fe₃O₄ (ICDD#01-088-0866), proving that the prepared composites possess a spinel structure. Furthermore, the shifting trend of the main diffraction peak is found to be consistent with the trend of the dopant ion radius size, as shown in the figure on the right, which shows the main peak (311) of the composite at XRD magnification. According to

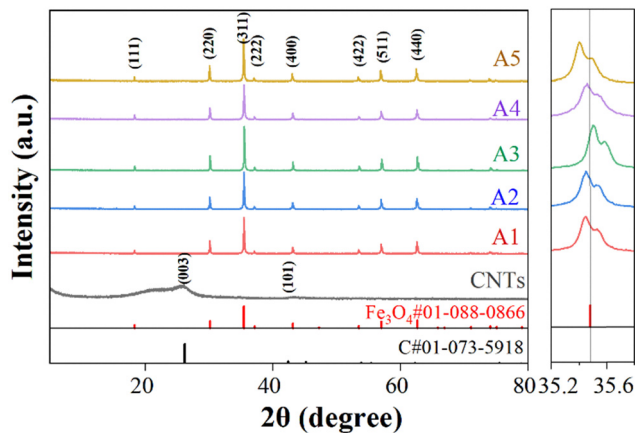


Fig. 1 XRD patterns and partially enlarged patterns of CNTs and $\text{Ni}_{0.4}\text{Zn}_{0.4}\text{Me}_{0.2}\text{Fe}_{1.94}\text{Cr}_{0.01}\text{O}_4/\text{CNT}$ samples.

ionic radius data, the radius gradient among Mg^{2+} (0.72 Å), Co^{2+} (0.745 Å), Ni^{2+} (0.69 Å), Cu^{2+} (0.73 Å), and Zn^{2+} (0.74 Å) induces lattice strain, resulting in the displacement of the (311) crystallographic plane observed by XRD. Specifically, the largest ionic radius (Zn^{2+}) causes lattice expansion, while the smallest (Ni^{2+}) leads to lattice contraction. The peaks of carbon nanotubes in ferrite composites are not obvious, and it is hypothesized that this may be because the intensity of the diffraction peaks of carbon nanotubes is much lower than that of ferrite; it could also be caused by a low carbon nanotube content.²⁰

3.2. Morphological analysis

Fig. 2(a) (1 and 2) and (3 and 4) show the transmission electron microscopy (TEM) images of the carbon nanotubes (CNTs) at 50 nm and 20 nm, respectively. Panels (b)–(f) display the scanning electron microscopy (SEM) images of $\text{Ni}_{0.4}\text{Zn}_{0.4}\text{Me}_{0.2}\text{Fe}_{1.94}\text{Cr}_{0.01}\text{O}_4/\text{CNTs}$ (Me = Mg, Co, Ni, Cu, and Zn). Under van

der Waals forces, the CNTs in Fig. 2(a) form rope-like bundles, measuring 10–20 nm in diameter and 5–10 μm in length. SEM analysis of the composites reveals that the ferrite sample particles remain larger than the CNTs even after ball milling. Consequently, the magnetic particles are embedded within the three-dimensional lattice formed by the CNTs, with good mixing observed between the CNTs and ferrite. Notably, Zn^{2+} ions retain a relatively large size under identical ball milling conditions. A common feature across all SEM micrographs is the formation of a CNT network structure, which contributes to electrical conductivity loss.

To prove the successful preparation of the composites, EDS analysis was performed, and the results are shown in Fig. 3. All elements are shown as densely and evenly distributed. Carbon nanotubes are not examined due to the low detection efficiency of the energy spectrometer for carbon, which would interfere with the accurate detection of carbon. Fig. 4 shows the elemental mapping and data summary of the sample obtained using an energy dispersive spectrometer (EDS), and the results verify that the sample was successfully prepared within the error range.

3.3. Magnetic performance analysis

The samples are tested using a vibrating sample magnetometer (VSM). The hysteresis loops of different composites are shown in Fig. 5. The hysteresis loops of all samples showed an S-shape, exhibiting soft magnetic properties. CNTs do not possess soft magnetic properties, so only ferrite is analyzed for magnetic properties.

Nickel–zinc ferrite has a typical spinel structure in which O^{2-} is cubically densely packed and metal cations are distributed in the tetrahedral (A) and octahedral (B) vacancies composed of oxygen ions.²¹ The magnetic properties of spinel ferrite are due to the magnetic moments of the magnetic ions at the tetrahedral and octahedral positions that are arranged in

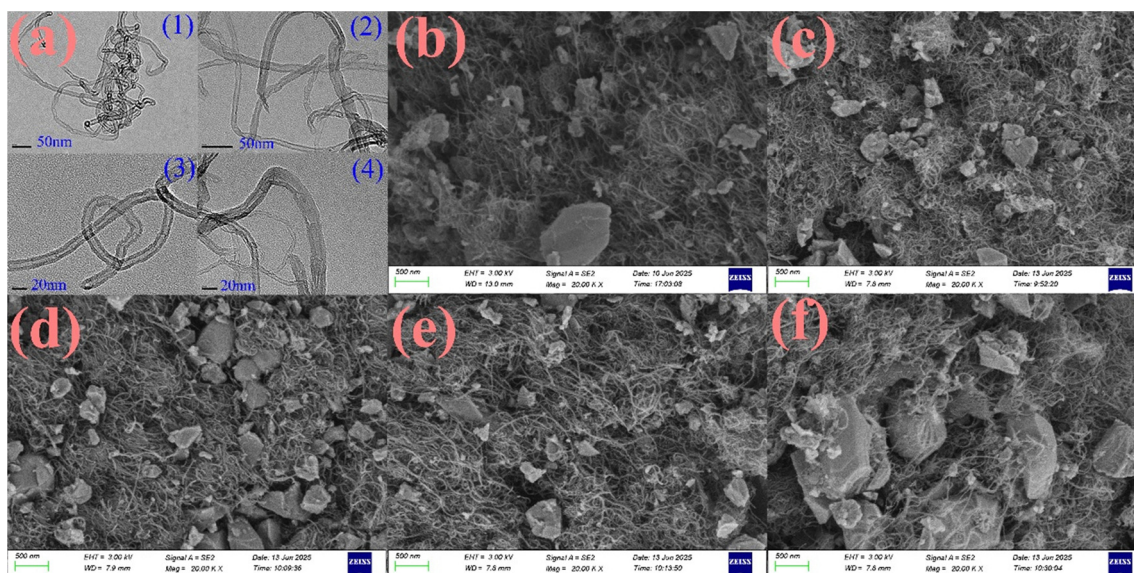


Fig. 2 (a) TEM images of CNTs. SEM images of $\text{Ni}_{0.4}\text{Zn}_{0.4}\text{Me}_{0.2}\text{Fe}_{1.94}\text{Cr}_{0.01}\text{O}_4/\text{CNT}$ samples with (b) A1, (c) A2, (d) A3, (e) A4 and (f) A5.

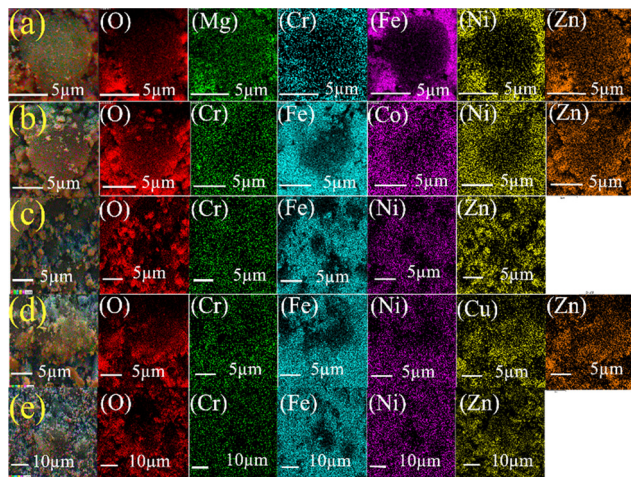


Fig. 3 Elemental mappings of $\text{Ni}_{0.4}\text{Zn}_{0.4}\text{Me}_{0.2}\text{Fe}_{1.94}\text{Cr}_{0.01}\text{O}_4/\text{CNT}$ samples with (a) A1, (b) A2, (c) A3, (d) A4 and (e) A5.

reverse parallel and do not completely cancel each other out. Therefore, the distribution of metal cations in the sublattice is closely related to the magnetic properties of the material.²²

The hysteresis lines show that A2 has the highest saturation magnetization intensity of 75.97 emu g^{-1} and A5 has the lowest saturation magnetization intensity of 61.53 emu g^{-1} . M_s is mainly related to the ionic magnetic moments and occupancy. Cu^{2+} , Ni^{2+} , and Co^{2+} occupy the octahedral (B) site, and Co^{2+} (3ub) is larger than Ni^{2+} (2ub) and Cu^{2+} (1.7ub), so A2 has the highest M_s .²³ Mg^{2+} and Zn^{2+} occupy the tetrahedral (A) site, and Mg^{2+} and Zn^{2+} are nonmagnetic elements with ionic magnetic moments of 0, so they have low M_s ; whereas Zn^{2+} has a larger radius than Mg^{2+} and has a larger effect on the tetrahedral (A) site, which has the lowest M_s .²⁴ H_c is a parameter of the internal stress, defects, grain size, and magnetic anisotropy.²⁵ Co^{2+} has a high magnetic anisotropy constant and therefore has the highest coercivity of 105.15 Oe; Zn^{2+} and Mg^{2+} are nonmagnetic ions and therefore have a lower coercivity of 35.29 Oe and 54.08 Oe, respectively.^{23,24}

3.4. Electromagnetic properties

To test the microwave absorption effect of the composites, the samples are analyzed with a vector network analyzer. The complex permittivity ($\epsilon_r = \epsilon' - j\epsilon''$) and complex permeability ($\mu_r = \mu' - j\mu''$) can respond to the properties of the sample, with the real part representing the ability to store energy and the imaginary part representing the ability to consume energy.²⁶ Thus, the attenuation of microwave energy can be expressed by the tangent of the dielectric loss angle ($\tan \delta_e$) and the tangent of the magnetic loss angle ($\tan \delta_\mu$). The electromagnetic parameter variation patterns of five ferrites and five composites within the 2–18 GHz frequency range are shown in Fig. 6. Fig. 6(a)–(f) displays the electromagnetic parameters of the five ion-doped ferrites, while panels (g)–(l) show the corresponding parameters for their composite counterparts. As illustrated in Fig. 6(a) and (g), the complex permittivity of the pristine ferrite remains nearly constant across the entire measured frequency

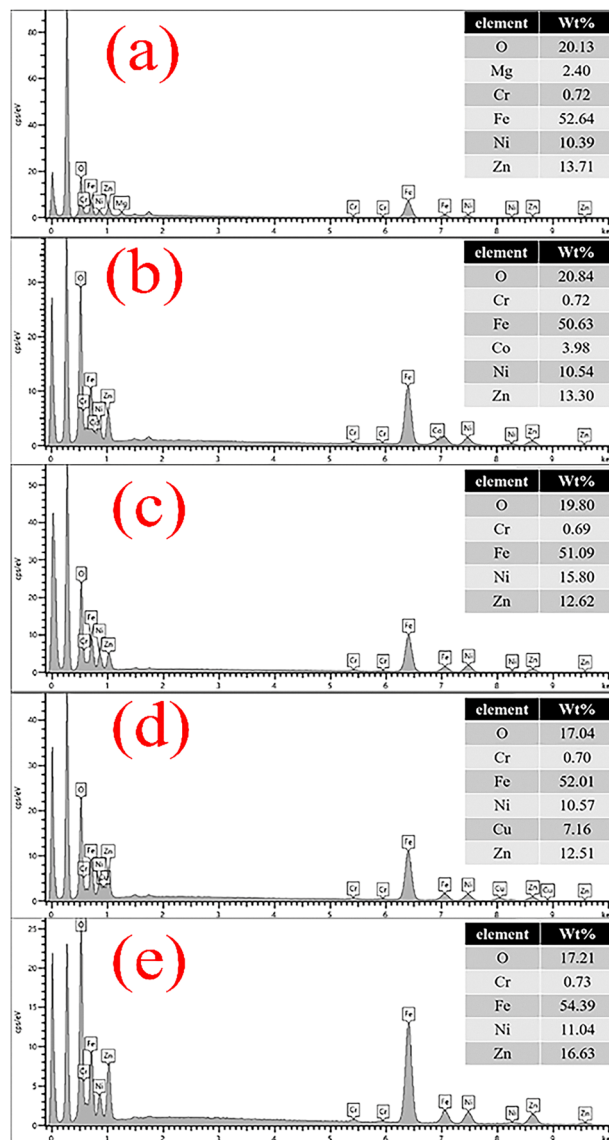


Fig. 4 Element mapping visualization of $\text{Ni}_{0.4}\text{Zn}_{0.4}\text{Me}_{0.2}\text{Fe}_{1.94}\text{Cr}_{0.01}\text{O}_4/\text{CNT}$ samples with (a) A1, (b) A2, (c) A3, (d) A4 and (e) A5.

range. In contrast, the composite exhibits significant permittivity reduction with increasing frequency. This behavior primarily stems from the composite's characteristic relaxation frequency being lower than the measurement range. Secondly, interfacial charge accumulation saturation may contribute to the sharp dielectric constant. Additionally, the dielectric loss peak observed at 14 GHz is attributed to strong interfacial polarization loss between the ferrite and carbon nanotubes.²⁷ In Fig. 6(g), the real part of the dielectric constant decreases with increasing frequency for all samples; A4 has the highest real part of the dielectric constant, and the variation of the actual dielectric constant in terms of the composition is caused by the porosity and grain size.²⁸ On the one hand, it is shown that copper lowers the sintering temperature and reduces the porosity.²⁹ On the other hand, copper doping may provide carriers and thus increase the material's polarization. In

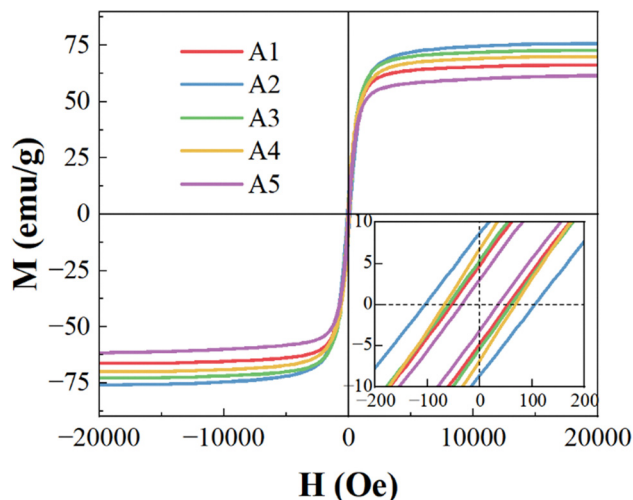


Fig. 5 Hysteresis loops of $\text{Ni}_{0.4}\text{Zn}_{0.4}\text{Me}_{0.2}\text{Fe}_{1.94}\text{Cr}_{0.01}\text{O}_4/\text{CNT}$ samples with (a) A1, (b) A2, (c) A3, (d) A4 and (e) A5 at room temperature.

Fig. 6(h), the increase in the imaginary part of the dielectric constant arises from relaxation and conduction losses.³⁰ In Fig. 6, the addition of carbon nanotubes (CNTs) significantly enhances both the real and imaginary parts of the dielectric constant. Eddy current losses generate natural and exchange resonances that underpin the magnetic permeability. Sample A4 exhibits the highest imaginary dielectric constant, indicating that Cu^{2+} doping effectively improves the material's dielectric loss capability. Furthermore, compared with other samples, Cu^{2+} doping introduces additional charge carriers. These carriers migrate to ferrite grain boundaries through hopping mechanisms, where their accumulation induces interfacial polarization. The resulting polarization loss arises from hysteresis in the electromagnetic dispersion behavior.³¹

Fig. 6(d), (e), (g) and (k) displays the variations in the real and imaginary parts of magnetic permeability. Both ferrites and composites exhibit identical trends, with all samples showing a decreasing permeability profile accompanied by fluctuations. As the frequency increases, the domain wall displacement within the material cannot keep pace with the changing magnetic field. Additionally, eddy currents generated at high frequencies oppose magnetic field variations, thus reducing permeability.³² At high frequencies, the imaginary part of the permeability is negative, which is the anti-magnetism caused by eddy current losses. According to Maxwell's equations, the movement of charges in the conducting network generates a new electric field, which produces a magnetic field that fails to cancel out, resulting in negative magnetic losses. Microwave absorption is affected by magnetic and dielectric losses.^{33,34} Fig. 6(c) and (i) presents the frequency dependence of the dielectric loss tangent for ferrites and their corresponding composites. The incorporation of carbon nanotubes (CNTs) enhances the dielectric loss in composites compared to pure ferrites. All composite samples exhibit similar profiles, with sample A4 demonstrating higher losses than other specimens below 14 GHz, whereas sample A2 shows progressively increasing losses above this frequency. Fig. 6(f) and (l) displays the

magnetic loss tangent *versus* frequency. The addition of CNTs reduces magnetic losses, with the observed trends aligning with variations in the imaginary part of magnetic permeability (μ''), consistent with eddy current dominance. In summary, at low frequencies, the difference between the angular tangent of magnetic loss and the tangent of dielectric loss is minimal, suggesting a collaborative interaction between the magnetic and dielectric losses. Conversely, at high frequencies, the tangent of the magnetic loss angle is lower than that of the dielectric loss angle, indicating that dielectric loss is the dominant factor.³⁵

3.5. Microwave absorption properties

Within the frequency spectrum spanning 2 to 18 GHz and thickness parameters ranging from 1 to 6 mm, the three-dimensional representation of the ferrite sample's microwave absorption properties, accompanied by the corresponding reflection loss (RL) contour plots, are illustrated in Fig. 7(a)–(k). The reflection loss (RL) is used to evaluate the microwave absorption characteristics of the material, and the $\text{RL} \leq -10$ dB (90% of the energy of the electromagnetic wave is absorbed) indicates effective absorption. Based on the transmission line theory, the following eqn (1) and impedance matching formulas (2) and (3) are derived.^{36–40}

$$\text{RL} = 20 \lg \left| \frac{Z_{\text{in}} - Z_0}{Z_{\text{in}} + Z_0} \right| \quad (1)$$

$$Z_0 = \sqrt{(\mu_0/\epsilon_0)} \quad (2)$$

$$Z_{\text{in}} = Z_0 \sqrt{\frac{\mu_r}{\epsilon_r}} \tanh \left[j \left(\frac{2\pi f t}{c} \right) \sqrt{\mu_r \epsilon_r} \right] \quad (3)$$

Z_{in} is the material input impedance, Z_0 is the free-space impedance, μ_0 is the vacuum permeability, ϵ_0 is the vacuum permittivity, f is the frequency, t is the material thickness, c is the speed of light, μ_r is the complex permeability, and ϵ_r is the complex permittivity. As illustrated in Fig. 7, the microwave absorption performance of the five doped ferrites exhibits significant variations. The Zn^{2+} -doped sample demonstrates optimal performance, achieving a peak reflection loss of -48.11 dB at 4 mm thickness and 6.48 GHz. This represents the strongest absorption among all specimens. The Ni^{2+} -doped sample ranks second with -37.71 dB absorption, while Cu^{2+} -, Co^{2+} -, and Mg^{2+} -doped ferrites exhibit comparatively weaker absorption. The exceptional performance of Zn^{2+} and Ni^{2+} samples at 4 mm thickness primarily stems from the optimized synergy between dielectric and magnetic loss mechanisms induced by these dopant ions. It can be seen in Fig. 8 that the RL of all samples first increases and then decreases with an increasing sample thickness. Sample A2 demonstrates superior bandwidth performance compared to other samples, exhibiting a bandwidth of 4.3 GHz at a thickness of 1.9 mm with a minimum reflection loss of -41.3 dB. In contrast, sample A4 achieves a bandwidth of 3.5 GHz at a reduced thickness of 1.4 mm, yet retains a lower minimum reflection loss of -46.32 dB. The microwave absorption

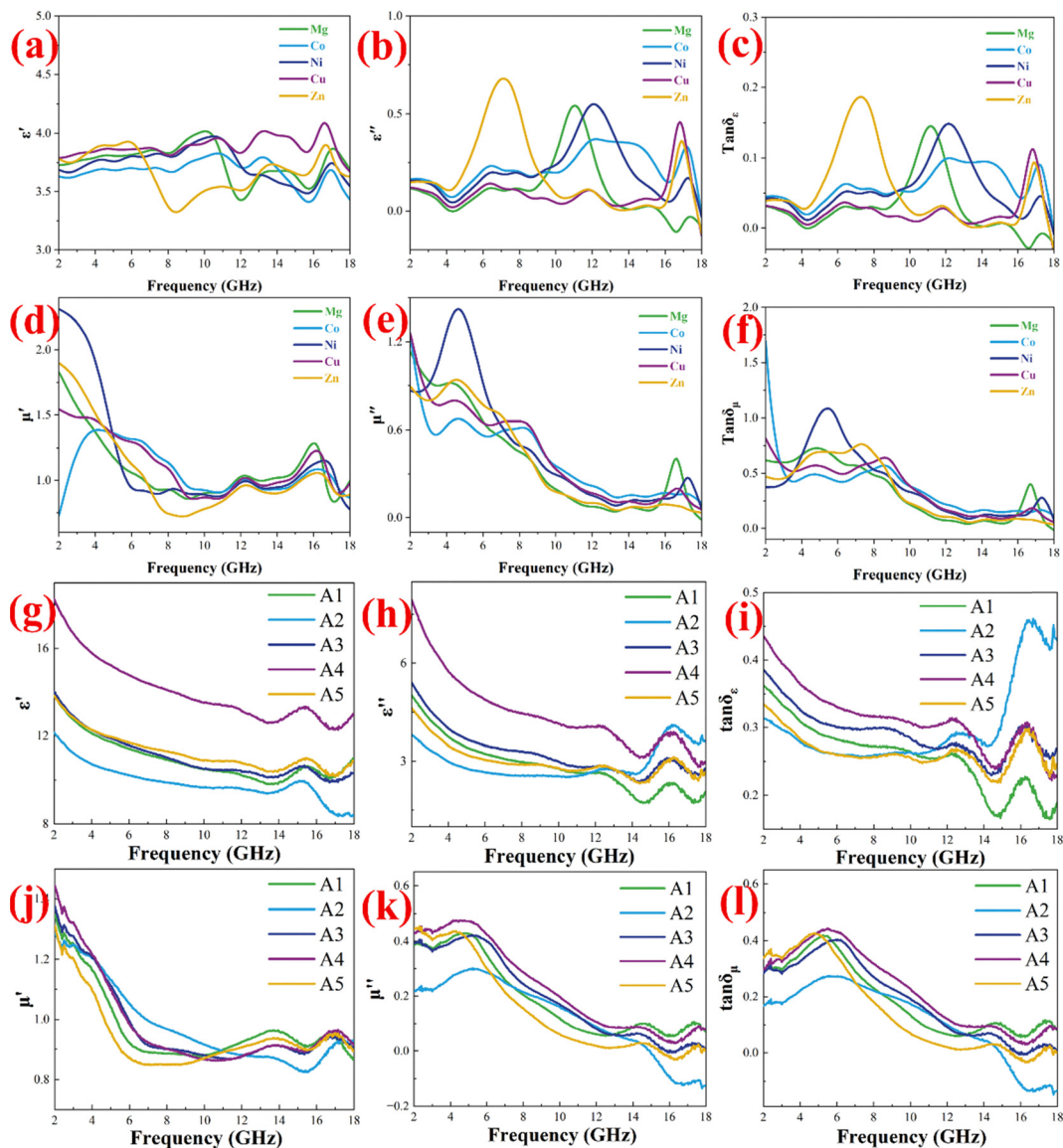


Fig. 6 Frequency dependence of (a) ϵ' , (b) ϵ'' , (c) μ' , (d) μ'' , (e) $\tan \delta_\epsilon$ and (f) $\tan \delta_\mu$ for $\text{Ni}_{0.4}\text{Zn}_{0.4}\text{Me}_{0.2}\text{Fe}_{1.94}\text{Cr}_{0.01}\text{O}_4$ and the frequency dependence of (g) ϵ' , (h) ϵ'' , (i) μ' , (j) μ'' , (k) $\tan \delta_\epsilon$ and (l) $\tan \delta_\mu$ for $\text{Ni}_{0.4}\text{Zn}_{0.4}\text{Me}_{0.2}\text{Fe}_{1.94}\text{Cr}_{0.01}\text{O}_4/\text{CNT}$ samples.

characteristics can be effectively modulated through the strategic selection of doped ions: cobalt ion doping contributes to bandwidth expansion, while copper ion doping facilitates further reduction in minimum reflection loss. The enhanced absorption performance can be attributed to the robust interface interaction between ferrite and carbon nanotubes, coupled with the increased material porosity induced by carbon nanotubes, which promotes electromagnetic wave reflection and scattering frequency enhancement.

Simultaneously, the theoretical matching thickness (t_m) was calculated using eqn (4).⁴¹

$$t_m = \frac{nc}{4f\sqrt{|\epsilon_r||\mu_r|}} \quad (4)$$

Fig. 8(c), (g), (k), (o) and (s) display the matching thickness versus frequency relationships for the five composites. The

quarter-wavelength cancellation mechanism represents one fundamental principle governing reflection loss (RL). When electromagnetic waves return from the reflector coated with the absorber film, they become attenuated and exhibit a 180° phase difference relative to waves penetrating the absorber-air interface. This phase cancellation occurs when the absorber thickness equals odd multiples of $\lambda/4$. The aforementioned mechanism accounts for the maximum RL shift induced by thickness variations. Additionally, multiple scattering and reflection at heterogeneous interfaces may enhance wave cancellation and microwave attenuation.⁴²

Impedance matching is evaluated based on the Z value, since the normalized impedance is an imaginary number that is difficult to calculate directly, and the modulus is used to study the reflection loss characteristics,⁴³ where $Z = 1$ indicates the optimal wave absorption performance. The closer Z is to 1,

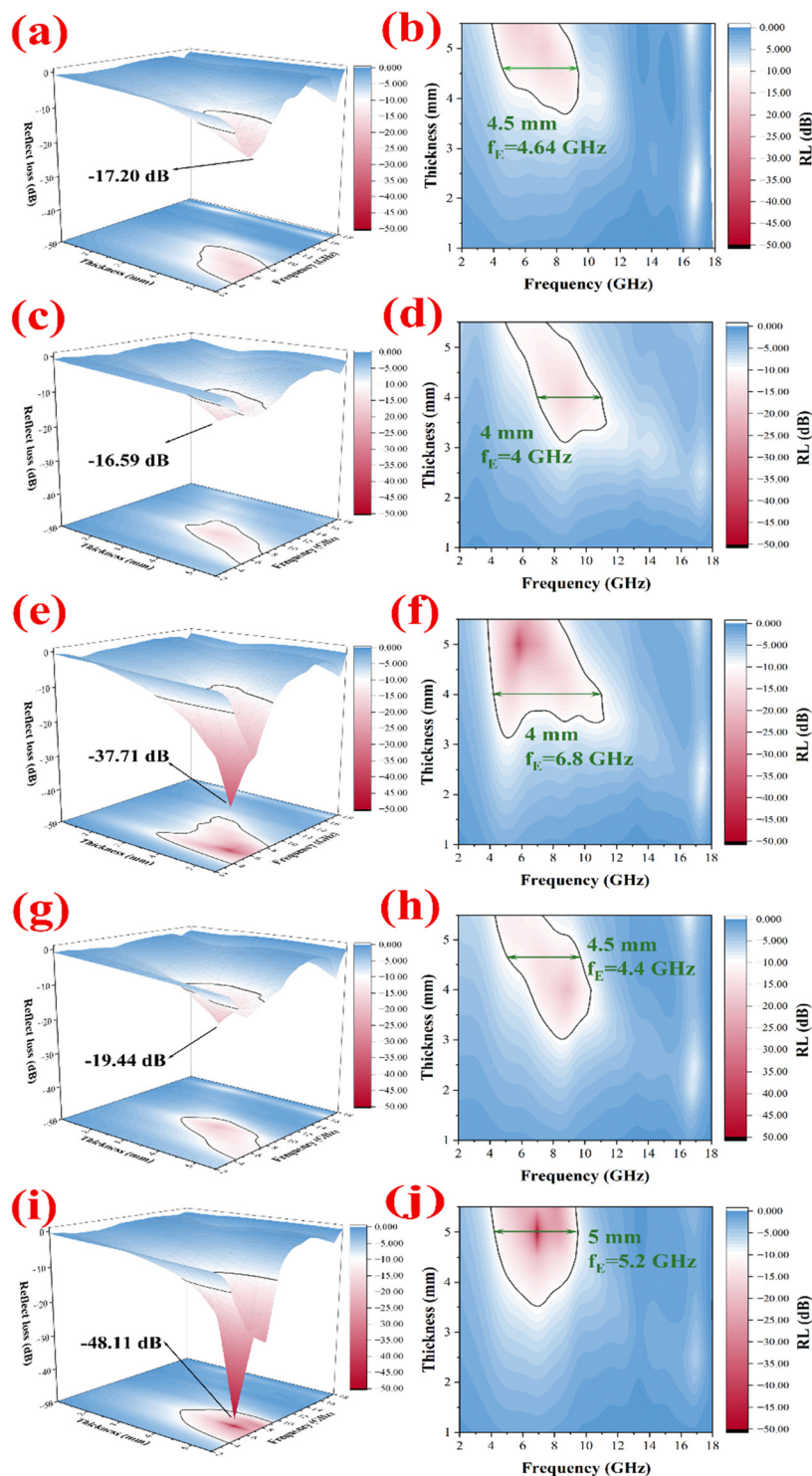


Fig. 7 3D images of RL images and contour RL maps of $\text{Ni}_{0.4}\text{Zn}_{0.4}\text{Me}_{0.2}\text{Fe}_{1.94}\text{Cr}_{0.01}\text{O}_4$ with (a) and (b) Mg, (c) and (d) Co, (e) and (f) Ni, (g) and (h) Cu, and (i) and (j) Zn.

the more incident waves can enter the absorbing material, which indicates excellent absorption properties in this frequency range,^{21,44} while Z values ranging from 0.8 to 1.2 signify satisfactory wave absorption performance. The calculation of the Z value is presented in eqn (4), and the impedance-matching contour plot is illustrated in Fig. 8.^{36,38,45}

In the contour plot, the orange curve corresponds to $Z = 1$, the green curve represents $Z = 0.8$, and the black curve denotes $Z = 1.2$. The comparative analysis of the wave absorption performance can be effectively conducted by examining the area enclosed between the green and black curves. It is not difficult to find that A2 has a larger regional area, resulting in

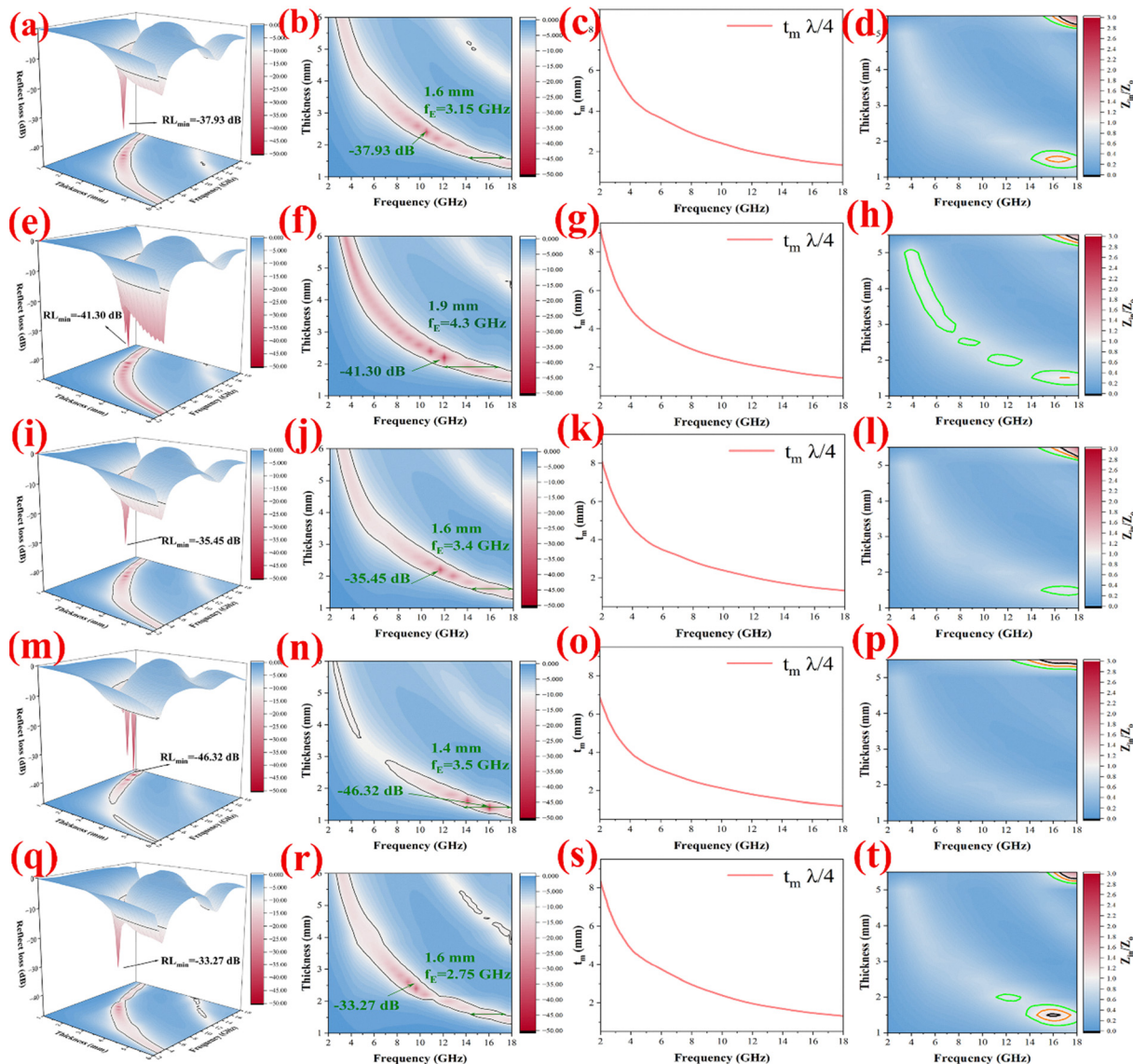


Fig. 8 RL(3D), RL(2D), t_m and Z_{in}/Z_0 contour maps of $\text{Ni}_{0.4}\text{Zn}_{0.4}\text{Me}_{0.2}\text{Fe}_{1.94}\text{Cr}_{0.01}\text{O}_4/\text{CNT}$ samples with (a)–(d) A1, (e)–(h) A2, (i)–(l) A3, (m)–(p) A4 and (q)–(t) A5.

good wave absorption properties of the sample.

$$Z = \frac{Z_{in}}{Z_0} = \left| \sqrt{\frac{\mu_r}{\epsilon_r}} \tanh \left[j \left(\frac{2\pi f t}{c} \right) \sqrt{\mu_r \epsilon_r} \right] \right| \quad (5)$$

Z is the material-normalized wave impedance. Microwave absorption has two absorption processes. First, the electromagnetic wave enters the composite material and is represented by the impedance matching. If the Z value is close to 1, it means that the electromagnetic waves can easily enter the material. Next, the microwaves are converted into thermal energy by dielectric and magnetic losses.⁴⁶

In the physically mixed composite system of divalent ion (Mg^{2+} , Co^{2+} , Ni^{2+} , Cu^{2+} , and Zn^{2+})-doped ferrites and carbon nanotubes (CNTs) prepared *via* the solid-state reaction, microwave absorption properties are synergistically regulated through three interconnected pathways:

Crystallite size reduction after ball milling elevates the interfacial density, which modulates the optimal absorption frequency⁴⁷ while promoting Schottky contact formation at ferrite–CNT heterointerfaces. This interfacial configuration induces a charge rearrangement to generate nanocapacitive structures, thereby enhancing interfacial polarization loss.⁴⁸

The CNT network functions as an antenna-like structure to facilitate multiple polarization mechanisms interfacial/dipolar polarization,⁴⁹ and scattering dissipation.⁵⁰ Its moderate conductivity dynamically balances defect-mediated effects—excessive conductivity obscures relaxation peaks, causing impedance mismatch, whereas optimized values cooperatively tune complex permittivity to the matching regime with interfacial polarization.⁵¹ Concurrently, CNT incorporation significantly increases the porosity and surface area, providing augmented relaxation loss mechanisms including interfacial/dipolar

polarization and multi-path dissipation.⁴⁹ Physical blending of ferrites and CNTs induces phase separation that generates additional defects,^{51,52} while conductive networks between MWCNTs coupled with interfacial/defect-induced polarization collectively contribute to dielectric loss.⁵³

Ion doping manifests dual influences: (i) ion-specific variations intensify magnetic loss (#8), and (ii) ionic radius disparities induce lattice strain to optimize dipolar polarization through charge symmetry disruption.⁴⁸ Concurrently, the diminished crystallite size (*e.g.*, Co²⁺ sample) amplifies lattice distortion, elevating the defect concentration to reinforce electron migration and conduction loss.⁵²

Conclusively, the Cu²⁺-doped composite achieves peak absorption of −46.32 dB at 16.05 GHz by balancing the conduction loss and polarization intensity, validating the efficacy of ion-screening strategies in regulating morphology-defect-electromagnetic parameter interrelationships.^{54,55}

To understand the dielectric loss mechanism, according to the Debye relaxation principle, the polarization relaxation process can be described by the Cole–Cole relaxation equation, which is as follows:⁵⁶

$$\left(\epsilon' - \frac{\epsilon_s + \epsilon_\infty}{2}\right)^2 + (\epsilon'')^2 = \left(\frac{\epsilon_s - \epsilon_\infty}{2}\right)^2 \quad (6)$$

where ϵ_s and ϵ_∞ are the static dielectric constant and the very high-frequency dielectric constant, respectively. Each hyperbola in the curve represents a Debye relaxation process, and the number and size of hyperbolas reflect the dielectric loss mechanism and capacity.⁵⁷ As illustrated in Fig. 9, interfacial defects arising from ferrite–carbon nanotube contacts induce distortion in the dielectric spectra. In the complex plane plot, the permittivity trajectory manifests as a characteristic arc with its chord along the real axis and center positioned below this axis.⁵⁸ When the arc center resides between the real axis and the curve, this feature signifies a single polarization mechanism:⁵⁹ the arc radius correlates with the polarization intensity, while the number of semicircles corresponds to distinct polarization types. The observed complete arc in the composite spectrum conclusively verifies the dominance of relaxation loss mechanisms.⁶⁰ As shown in Fig. 9, all samples have the same

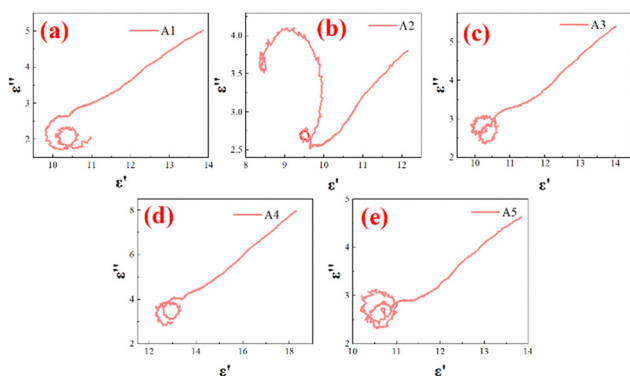


Fig. 9 Cole–Cole plots of Ni_{0.4}Zn_{0.4}Me_{0.2}Fe_{1.94}Cr_{0.01}O₄/CNT samples with (a) A1, (b) A2, (c) A3, (d) A4 and (e) A5.

kind of polarization relaxation with different degrees. The trend shown in Fig. 9(b) is different from that in the other samples, which is attributed to the increase in the imaginary part of the dielectric constant of A2. The Cole–Cole curve response to the polarization curve is not ideal. The curves are distorted, suggesting that other loss mechanisms exist besides the dielectric loss effect due to Debye relaxation.³¹ The aggregation of charges at multiple heterogeneous interfaces in a composite material under the action of electromagnetic fields leads to the generation of interfacial polarization.^{31,35,61} Fig. 2 reveals a phase-separated structure with ferrite embedded in carbon nanotubes, where heterogeneous interfaces serve as physical carriers for charge accumulation. Comparative analysis of the intrinsic permittivity of ferrite and the composite demonstrates significant enhancement in the dielectric constant, indicating superior electromagnetic wave storage capability and pronounced loss characteristics.⁶² Although the minor permittivity increase induced by interfacial charge accumulation is not directly visible in the data, the slope variation suggests a dielectric peak below 2 GHz. Beyond this frequency, the monotonic decrease in permittivity implies saturated interfacial charge accumulation. Concurrently, the relaxation features in $\tan\delta$ confirm that carbon nanotube incorporation induces multiple polarization mechanisms. Moreover, many defects in carbon nanotubes can act as dipole polarization centers and form dipole polarization.⁶³ In addition, the $\epsilon' - \epsilon''$ curves of the composites tail into a straight line, indicating the presence of conduction losses.^{35,37}

The origin of the magnetic loss of samples could be evaluated through the eddy current factor (C_0) parameter, which could be calculated from the complex permeability using eqn (7).⁶⁴

$$C_0 = \frac{\mu''}{(\mu')^2 f} \quad (7)$$

Based on the skin effect criterion, the C_0 value criterion was employed to analyze the contribution of eddy current losses to magnetic loss mechanisms in the composite material. A constant C_0 value indicates predominantly eddy current losses. Fig. 10(a) reveals that all C_0 curves transition from stability to a significant decline within the 2–8 GHz range, confirming that while eddy current losses dominate, they are effectively suppressed. Above 8 GHz, there are obvious oscillation characteristics in the imaginary part of the magnetic permeability, which are attributed to the magnetic loss mechanism involving exchange and natural resonance.⁶⁵ Given the substantial volume disparity between ferrite and carbon nanotubes, natural resonance is identified as the dominant loss mechanism in the high-frequency regime.^{66,67}

Impedance matching and attenuation constant are the keys to microwave absorption.⁴⁶ Fig. 10(b) illustrates the attenuation constant *versus* frequency, and the attenuation constant α can be calculated by the following eqn (8).⁴⁰

$$\alpha = \frac{\sqrt{2}\pi f}{c} \sqrt{(\mu''\epsilon'' - \mu'\epsilon')^2 + (\epsilon'\mu'' + \epsilon''\mu')^2} \quad (8)$$

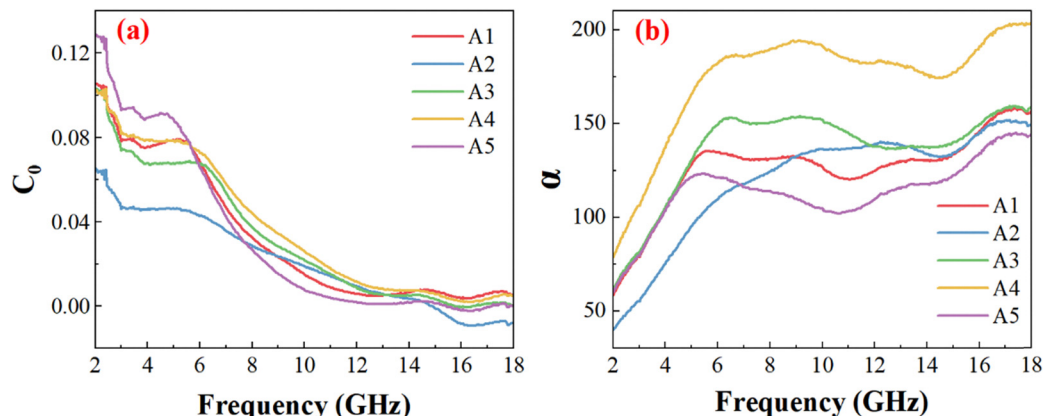


Fig. 10 (a) C_0 and (b) α curves of $\text{Ni}_{0.4}\text{Zn}_{0.4}\text{Me}_{0.2}\text{Fe}_{1.94}\text{Cr}_{0.01}\text{O}_4/\text{CNTs}$ samples.

Fig. 10(b) clearly shows that all these attenuation coefficients increase with increasing frequency, indicating that ferrite composites have excellent electromagnetic wave attenuation capability. Among them, the attenuation constant of A4 far exceeds that of the other samples, indicating the strongest EMW attenuation capability among all the samples. The attenuation constant of A2 is lower than that of the other samples at low frequencies, but at high frequencies, there is a substantial increase, verifying a good impedance match at high frequencies.

Fig. 11 shows a comprehensive comparison of the five modified specimens that systematically demonstrate that microwave absorption characteristics, including both RL_{\min} and EAB_{\max} parameters, can be effectively engineered through the strategic selection of dopant ion species. Through comparative analysis of ferrites and their corresponding composites, it is evident that specific ion doping significantly influences microwave absorption before carbon nanotube (CNT) incorporation. However, the practical application of unmodified ferrites is limited by their excessive thickness. Upon CNT

composite formation, both Cu^{2+} - and Co^{2+} -doped ferrites demonstrate enhanced compatibility with the carbon matrix. Considering the critical parameters—including thickness reduction, absorption peak intensity, and effective bandwidth—the Cu^{2+} -doped ferrite composite exhibits optimal overall performance, achieving superior impedance matching and attenuation characteristics.

In summary, in ferrite composites, ferrite generates magnetic loss through natural resonance and eddy current loss; ferrite and carbon nanotubes generate dielectric loss through interfacial polarization and carbon nanotubes' dipole polarization; and ferrite and carbon nanotubes form a three-dimensional lattice, and electron migration causes conduction loss.⁶⁸ The synergistic effect between the losses can improve the microwave absorption properties of the material.⁶⁹ Taken together, Cu^{2+} doped has the best impedance matching and absorption band, the best electromagnetic attenuation capability, and exhibits the best electromagnetic wave absorption performance among the five samples.

4. Conclusions

$\text{Ni}_{0.4}\text{Zn}_{0.4}\text{Me}_{0.2}\text{Fe}_{1.94}\text{Cr}_{0.01}\text{O}_4/\text{CNT}$ composites (Me = Mg, Co, Ni, Cu, and Zn) were synthesized *via* solid-state/ultrasonic methods. The transition metal cation species in spinel ferrites serve as a critical determinant in modulating both magnetic response and microwave dissipation characteristics: saturation magnetization (M_s) scales with ionic magnetic moments, while dopants concurrently tune CNTs' permittivity and ferrite permeability. This dual modulation enables balanced impedance matching ($Z_{\text{in}}/Z_0 \approx 1$) and high energy conversion (>90%) through tunable dielectric/eddy current losses. Specifically, Cu^{2+} doping achieves an RL_{\min} of -46.32 dB at 1.4 mm thickness. Strategic ion-selection thus enables synergistic design of ultrathin absorbers with dual-optimized attenuation and bandwidth.

Author contributions

Zhihao Geng: data curation; investigation; writing – original draft; and Writing-review & editing. Yujie Yang: funding

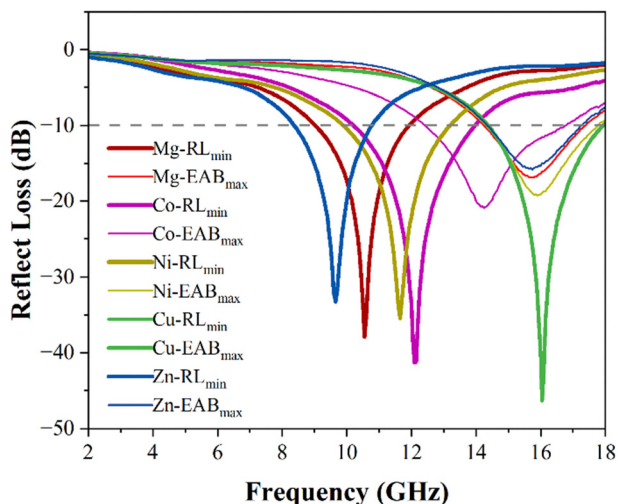


Fig. 11 Comparison of the EM wave absorption properties of $\text{Ni}_{0.4}\text{Zn}_{0.4}\text{Me}_{0.2}\text{Fe}_{1.94}\text{Cr}_{0.01}\text{O}_4/\text{CNT}$ samples.

acquisition. Zhenyu Zhang: methodology. Hao Li: methodology. Hongyu Ding: methodology.

Conflicts of interest

The authors declare that they have no known competing financial interests or personal relations that could have appeared to influence the work reported in this paper.

Data availability

The data that support the findings of this study are available on request from the corresponding author. The data are not publicly available due to privacy or ethical restrictions.

References

- P. Bandara and D. O. Carpenter, *Lancet Planet. Health*, 2018, **2**, E512–E514.
- M. Green, L. Tian, P. Xiang, J. Murowchick, X. Tan and X. Chen, *Mater. Chem. Front.*, 2018, **2**, 1119–1125.
- H. Pang, Y. Duan, L. Huang, L. Song, J. Liu, T. Zhang, X. Yang, J. Liu, X. Ma, J. Di and X. Liu, *Composites, Part B*, 2021, **224**, 109173.
- R. S. Yadav and I. Kuritka, *Crit. Rev. Solid State Mater. Sci.*, 2024, **49**, 371–407.
- V. G. Kostishin, I. M. Isaev and D. V. Salogub, *Polymers*, 2024, **16**, 1003.
- S. A. Habib, S. A. Saafan, T. M. Meaz, M. A. Darwish, D. Zhou, M. U. Khandaker, M. A. Islam, H. Mohafez, A. V. Trukhanov, S. V. Trukhanov and M. K. Omar, *Nanomaterials*, 2022, **12**, 931.
- Z. Ma, C. Mang, X. Weng, Q. Zhang, L. Si and H. Zhao, *Materials*, 2018, **11**, 590.
- S. Sheykhmoradi, A. Ghaffari, A. Mirkhan, G. Ji, S. Tan and R. Peymanfar, *Dalton Trans.*, 2024, **53**, 4222–4236.
- R. Peymanfar and F. Azadi, *J. Mater. Sci – Mater. Electron.*, 2020, **31**, 9586–9594.
- X. Huang, J. Zhang, M. Lai and T. Sang, *J. Alloys Compd.*, 2015, **627**, 367–373.
- H. Wei, W. Li and K. Bachagha, *Carbon*, 2024, **217**, 118651.
- H. Yang, T. Ye, Y. Lin, J. Zhu and F. Wang, *J. Alloys Compd.*, 2016, **683**, 567–574.
- P. Hemmati-Eslamli, A. Habibi-Yangjeh, Y. Akinay and T. Cetin, *J. Photochem. Photobiol., A*, 2023, **443**, 114862.
- M. S. Mustafa, R. A. S. Azis, N. H. Abdullah, I. Ismail and I. R. Ibrahim, *Sci. Rep.*, 2019, **9**, 15523.
- M. Chahar, S. Dabas and O. P. Thakur, *Ceram. Int.*, 2022, **48**, 5352–5360.
- H. Wang, X. Xiao, S. Zhai, C. Xue, G. Zheng, D. Zhang, R. Che and J. Cheng, *Nano-Micro Lett.*, 2025, **17**, 19.
- S. M. Seyedian, A. Ghaffari, A. Mirkhan, G. Ji, S. Tan, S. Ghorbanian-Gezaforodi and R. Peymanfar, *Ceram. Int.*, 2024, **50**, 13447–13458.
- R. Peymanfar and F. Fazlalizadeh, *Chem. Eng. J.*, 2020, **402**, 126089.
- R. Peymanfar, S. Javanshir, M. R. Naimi-Jamal, A. Cheldavi and M. Esmkhani, *J. Electron. Mater.*, 2019, **48**, 3086–3095.
- H. Gao, J.-y. Shen, H. Zhang, X. Gao, X.-n. Tang, L.-h. Zhu and T. Si, *Ceram. Int.*, 2025, **51**, 1499–1507.
- J. Song, Y. Gao, G. Tan, Q. Man and Z. Wang, *Ceram. Int.*, 2022, **48**, 22896–22905.
- G. M. Shweta, L. R. Naik, R. B. Pujar and S. N. Mathad, *Mater. Chem. Phys.*, 2021, **257**, 123825.
- C. Chen, Y. Yang, Y. Zhang, D. Chen, H. Li, Y. Meng and Z. Zhang, *Mater. Today Commun.*, 2023, **37**, 107497.
- N. Kavitha and P. Manohar, *J. Supercond. Novel Magn.*, 2016, **29**, 2151–2157.
- Y. Matsuura, N. Kitai, S. Hosokawa and J. Hoshijima, *J. Magn. Magn. Mater.*, 2016, **411**, 1–6.
- C.-Y. Chen, N.-W. Pu, Y.-M. Liu, S.-Y. Huang, C.-H. Wu, M.-D. Ger, Y.-J. Gong and Y.-C. Chou, *Composites, Part B*, 2017, **114**, 395–403.
- T. Guo, S. Chang and Y. Akinay, *Synth. Met.*, 2020, 266.
- Y. Sani, R. a S. Azis, I. Ismail, Y. Yaakob, M. K. A. Karim, J. Mohammed and B. M. Alhaji, *Diamond Relat. Mater.*, 2023, **139**, 110325.
- R. M. Sundaram, A. Sekiguchi, M. Sekiya, T. Yamada and K. Hata, *R. Soc. Open Sci.*, 2018, **5**, 180814.
- A. Fahimi, P. Fakharian, A. Mirakhan, A. Farahani, Z. Zhou, Y. Zhao and R. Peymanfar, *J. Mater. Chem. C*, 2024, **12**, 12535–12548.
- Y.-Y. Wang, Y. Song, W.-J. Sun, K. Dai, D.-X. Yan and Z.-M. Li, *J. Mater. Sci. Technol.*, 2022, **102**, 115–122.
- Y. Cai, H. Yu, L. Cheng, Y. Yuan, S. Guo, Z. Hu, Y. Wang, D. Chen, J. Liu and H. Yuan, *Ceram. Int.*, 2024, **50**, 51128–51138.
- P. Negi, A. Gupta, P. Kumar, N. Rani and A. Kumar, *Mater. Chem. Phys.*, 2024, **320**, 129448.
- W. Q. Guo, B. Hong, J. C. Xu, Y. B. Han, X. L. Peng, J. Li, H. W. Chen and X. Q. Wang, *Ceram. Int.*, 2025, **51**, 764–776.
- Y.-N. Gao, Y. Wang, T.-N. Yue and M. Wang, *Composites, Part B*, 2023, **249**, 110402.
- Q. Chang, Z. Xie, G. Chen, Z. Li, Y. Duan, B. Shi and H. Wu, *J. Mater.*, 2025, **11**, 100927.
- M. A. Aslam, K. Hu, W. Ding, A. Hassan, Y. Bian, K. Qiu, Q. Liu and Z. Sheng, *Ceram. Int.*, 2021, **47**, 27496–27502.
- M. Ning, B. Kuang, Z. Hou, L. Wang, J. Li, Y. Zhao and H. Jin, *Appl. Surf. Sci.*, 2019, **470**, 899–907.
- M. F. Elmahaishi, R. a S. Azis, I. Ismail and F. D. Muhammad, *J. Mater. Res. Technol.*, 2022, **20**, 2188–2220.
- X. Wang, B. Wang, S. Wei, Y. Liang, Y. Wang, L. Li and Z. Liu, *Colloids Surf., A*, 2023, **671**, 131678.
- Y. Cao, A. M. Mohamed, M. Mousavi and Y. Akinay, *Mater. Chem. Phys.*, 2021, 259.
- H. Rezaei, F. Soltani-Mohammadi, H. Dogari, H. Ghafuri and R. Peymanfar, *Nanoscale*, 2024, **16**, 18962–18975.
- H. Xu, X. Yin, M. Zhu, M. Han, Z. Hou, X. Li, L. Zhang and L. Cheng, *ACS Appl. Mater. Interfaces*, 2017, **9**, 6332–6341.

- 44 S. Liu, J. Wang, B. Zhang, X. Su, X. Chen, Y. Chen, H. Yang, Q. Wu and S. Yang, *Carbon*, 2024, **219**, 118802.
- 45 M. Yu, Y. Zheng, C. Liao and X. Liu, *J. Alloys Compd.*, 2024, **983**, 173956.
- 46 M. Z. Ashfaq, A. Ashfaq, M. K. K. Majeed, A. Saleem, S. Wang, M. Ahmad, M. M. Hussain, Y. Zhang and H. Gong, *Ceram. Int.*, 2022, **48**, 9569–9578.
- 47 H. Zhang, J. Cheng, H. Wang, Z. Huang, Q. Zheng, G. Zheng, D. Zhang, R. Che and M. Cao, *Adv. Funct. Mater.*, 2022, **32**, 2108194.
- 48 L. Liang, W. Gu, Y. Wu, B. Zhang, G. Wang, Y. Yang and G. Ji, *Adv. Mater.*, 2022, **34**, 2106195.
- 49 R. Peymanfar, S. Javanshir, M. R. Naimi-Jamal and S. H. Tavassoli, *J. Mater. Sci.*, 2021, **56**, 17457–17477.
- 50 F. Fazlalizadeh, Z. Nezafat, S. Javanshir and R. Peymanfar, *Ind. Crops Prod.*, 2025, **229**, 120954.
- 51 G. Chen, L. Zhang, B. Luo and H. Wu, *J. Colloid Interface Sci.*, 2022, **607**, 24–33.
- 52 R. Peymanfar, P. Mousivand and A. Mirkhan, *Energy Technol.*, 2024, **12**, 2300684.
- 53 Z. Wu, H.-W. Cheng, C. Jin, B. Yang, C. Xu, K. Pei, H. Zhang, Z. Yang and R. Che, *Adv. Mater.*, 2022, **34**, 2107538.
- 54 Y. Wu, Y. Zhao, M. Zhou, S. Tan, R. Peymanfar, B. Aslibeiki and G. Ji, *Nano-Micro Lett.*, 2022, **14**, 171.
- 55 X. Guan, Z. Yang, Y. Zhu, L. Yang, M. Zhou, Y. Wu, L. Yang, T. Deng and G. Ji, *Carbon*, 2022, **188**, 1–11.
- 56 H. Yan, Y. Guo, X. Bai, J. Qi, X. Zhao, H. Lu and L. Deng, *Appl. Surf. Sci.*, 2023, **633**, 157602.
- 57 X. Wang, S. Wei, Y. Yuan, R. Li, Y. Wang, Y. Liang, B. Wang and C. Dong, *J. Alloys Compd.*, 2022, **909**, 164676.
- 58 K. S. Cole and R. H. Cole, *J. Chem. Phys.*, 1941, **9**, 341–351.
- 59 E. Selseleh-Zakerin, A. Mirkhan, M. Shafiee, M. Alihoseini, M. Khani, B. Shokri, S. H. Tavassoli and R. Peymanfar, *Langmuir*, 2024, **40**, 12148–12158.
- 60 H. Dogari, H. Ghafuri and R. Peymanfar, *Adv. Sustainable Syst.*, 2025, **9**, 2400793.
- 61 T. H. Ting, R. P. Yu and Y. N. Jau, *Mater. Chem. Phys.*, 2011, **126**, 364–368.
- 62 H. Yang, H. Wang, X. Dong, K. Zhu, X. Zhou and S. Zhai, *New J. Chem.*, 2025, **49**, 3890–3901.
- 63 Z. Bi, L. Yao, X. Wang, L. Zeng, S. Zhang, J. Yan, W. Zhao, Y. Wang, Z. Zhang and J. Yun, *J. Alloys Compd.*, 2022, **926**, 166821.
- 64 P. Yin, L. Zhang, P. Sun, J. Wang, X. Feng, Y. Zhang, J. Dai and Y. Tang, *Ceram. Int.*, 2020, **46**, 13641–13650.
- 65 J. Chen, H.-H. Wang, Q.-D. An, Z.-Y. Xiao, X.-L. Dong, K.-R. Zhu and S.-R. Zhais, *New J. Chem.*, 2024, **48**, 1172–1181.
- 66 F. Hu, H. Nan, M. Wang, Y. Lin, H. Yang, Y. Qiu and B. Wen, *Ceram. Int.*, 2021, **47**, 16579–16587.
- 67 X. Zhao, Y. Huang, X. Liu, J. Yan, L. Ding, M. Zong, P. Liu and T. Li, *J. Colloid Interface Sci.*, 2022, **607**, 192–202.
- 68 R. Shu, G. Zhang, J. Zhang, X. Wang, M. Wang, Y. Gan, J. Shi and J. He, *J. Alloys Compd.*, 2018, **736**, 1–11.
- 69 M. Rostami, M. Moradi, R. S. Alam and R. Mardani, *Mater. Res. Bull.*, 2016, **83**, 379–386.